

Capturing Dynamic Core Reconstruction and Ligand Desorption of Atomically Precise Ag Nanoclusters with Machine Learning Force Field

Fang Sun and Qing Tang*



Cite This: <https://doi.org/10.1021/jacs.5c15207>



Read Online

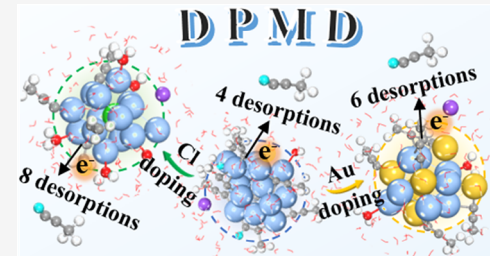
ACCESS |

Metrics & More

Article Recommendations

Supporting Information

ABSTRACT: Atomically precise silver nanoclusters (NCs) protected by alkynyl ligands represent an emerging class of electrocatalysts demonstrating high activity and selectivity in reactions, such as CO₂ electroreduction. However, their dynamic structural evolution mechanisms under electrochemical operating conditions remain elusive. Conventional experimental characterization faces a grand challenge to resolve atomic-scale dynamic processes, while *ab initio* molecular dynamics (AIMD) simulations are solely confined to picosecond time scales, insufficient for capturing the dynamics of evolution over longer times. Combining multiscale constant potential simulations and a deep potential molecular dynamics (DPMD) scheme, here we developed a high-accuracy machine learning force field within the deep-learning framework to elucidate the electrochemical structural evolution in all-alkynyl-protected Ag₁₅ NC and its doped systems (Ag₈Au₇, Ag₉Cu₆, and Ag₁₄Cl NCs). We found that the metal cores of all NCs undergo a transition from octahedral to disordered, accompanied by partial or complete cleavage of surface alkynyl ligands. The dopants critically modulate the stability by regulating desorption pathways, with Ag₉Cu₆ NC exhibiting exceptional resistance to dissociation due to robust Cu–C bonding. Our nanosecond-level DPMD simulations based on trained machine learning force fields further confirmed that doping dramatically affects the number of desorbed alkyne ligands (4 for Ag₁₅, 6 for Ag₈Au₇, and 8 for Ag₁₄Cl) and the degree of core ordering, and a long-term simulation of >2000 ps was crucial for capturing the dynamic electrochemical interface. This study established the first quantitative correlation between electrochemical interface dynamics and doping effects, providing a theoretical paradigm for designing highly stable atomically precise catalysts.



INTRODUCTION

Ultrasmall atomically precise metal nanoclusters (NCs) stabilized by organic ligands exhibit significantly different electrical and optical properties from bulk metals and nanocrystals, and have broad application prospects in fields such as nanocatalysis, biosensing, and molecular recognition.¹ For example, numerous cutting-edge experimental studies have shown that atomically precise Ag NCs, as an emerging class of electrocatalytic materials, have demonstrated excellent catalytic activity and high selectivity in key electrochemical conversion processes such as the hydrogen evolution reaction (HER), oxygen reduction reaction (ORR), carbon dioxide reduction reaction (CO₂RR), and nitrate reduction reaction (NO₃⁻RR).^{2–18} Recently, intensive research efforts have turned to elucidating the dynamic nature of NCs under reaction conditions to establish the structure–reactivity relationships.^{1,19} Under realistic electrocatalytic conditions, factors such as applied electric potential or the electrolyte environment can induce dynamic reconstruction of catalytic surfaces, leading to significant deviations in structural and catalytic behavior compared to the pristine surfaces.^{20–24} It is worth noting that ligand-protected NCs often undergo motion of the ligand shell and dynamic structural changes of the metal

core under reaction conditions.^{25–27} All of these impact catalytic activity. Therefore, understanding the structure and dynamics of NC catalysts is needed for improving the performance. Advanced techniques have recently been used to characterize the atomic-scale structures of NCs. For instance, aberration-corrected scanning transmission electron microscopy can provide dynamic structural information regarding the size, position, and chemical composition of metal NCs.^{28,29} In situ spectroscopy technology can offer information on the coordination environment of the NC catalysts during the reaction process.^{30,31} Ma et al. employed a single nanoparticle collision electrochemical method to conduct real-time monitoring of Au₂₅(PPh₃)₁₀(SC₂H₄Ph)₅Cl₂₊ NC in the ORR process.³² They demonstrated that a fully ligand-protected Au₂₅²⁺ NC was activated by ligand removal at the beginning of the ORR

Received: September 1, 2025

Revised: November 12, 2025

Accepted: November 25, 2025

and may deactivate due to the occasional return of desorbed ligands, giving rise to reversible “ON–OFF” switches.

Although the above experimental methods can capture the catalytic dynamic information, it is still hard to get an atomically detailed picture of the complex structural evolution. Alternatively, *ab initio* molecular dynamics (AIMD), which combines electronic structure calculations and configuration sampling, is a powerful tool for elucidating the underlying mechanisms of dynamic catalysis. However, AIMD is computationally expensive and can only simulate hundreds of atoms over several picoseconds (ps).^{33–36} Classical molecular dynamics (MD) based on force fields can be used for large-scale simulations, but it lacks reliability for simulating reactions involving changes in chemical bonds. Thus, one main challenge is to develop an efficient approach that allows for the computation of catalytic processes at much greater sizes and time scales while maintaining the *ab initio* accuracy. The recently developed Deep Potential Molecular Dynamics (DPMD), based on deep neural networks, can combine the computational accuracy of AIMD with the simulation scale and speed of classical MD, making it feasible to achieve reliable molecular simulations for large-scale systems.^{24,37–39}

Compared with the widely studied Au NCs, Ag NCs possess cost advantages and also exhibit high electrocatalytic activity. However, due to their relatively higher metallic reactivity and intrinsic susceptibility to oxidation, they may degrade under long-term electrochemical operating conditions. The stability is crucial for promoting subsequent reactions, and an ideal electrocatalyst should possess high activity, high selectivity, and good stability. Therefore, our primary task is to clarify the dynamic evolution mechanism of silver NCs during the electrocatalytic process. Here, we selected the homoleptic alkynyl-protected $[Ag_{15}(C\equiv C-tBu)_{12}]^+$ NC¹⁴ (abbreviated as Ag₁₅) as the model catalyst. To overcome the limitations of conventional static models and short time-scale simulations, we developed a high-accuracy machine learning force field (MLFF) within the deep-learning framework. The iteratively trained force field parameters using structures obtained via AIMD simulations enable nanosecond-scale DPMD calculations. By systematically investigating pristine Ag₁₅ NC and doped variants of this NC (Ag₈Au₇, Ag₉Cu₆, and Ag₁₄Cl), we unveiled the following phenomenon: (1) the potential-driven metal-core distortion and ligand restructuring pathways; (2) the dopant-dependent modulation mechanisms governing the ligand dissociation kinetics; and (3) the correlation between long-time scale evolution of ligand detachment dynamics and structural integrity. This work establishes a theoretical framework for evaluating dynamic stability and rationally engineering Ag NC catalysts to achieve high activity and stability.

RESULTS AND DISCUSSION

Unconstrained AIMD Simulations. It has been experimentally observed that the Ag₁₅ NC is an excellent electrocatalyst for CO₂RR, exhibiting high Faraday efficiency to generate CO products.¹⁴ Based on the resolved single-crystal diffraction structure, we first constructed an explicit solvent model and performed unrestricted AIMD simulations to investigate the structural tolerance of the Ag₁₅ NC in an alkaline electrolyte (first without any applied potential). As shown in Figure S1, the Ag₁₅ NC was placed in a 22 Å × 22 Å × 30 Å cubic unit cell, surrounded by 250 water molecules. In the water layer, one explicit Na atom and two F atoms are

placed to form an ionic solvation system, so as to simulate the alkaline media (pH 14) and balance the +1 charge of the cluster. Given the high computing cost of the AIMD simulations, all experimental $-C\equiv C-tBu$ ligands are simplified with $-C\equiv C-CH_3$. The initial structural relaxation indicated that the regular octahedral metal core of the Ag₁₅ cluster only undergoes slight changes, while one of the 12 alkynyl ligands that were previously coordinated to the Ag metal in a tricoordination (μ_3) manner changed to a dimeric coordination (μ_2). To differentiate the coordination modes of the ligands, we marked the C atoms in the μ_3 , μ_2 , and μ_1 modes as gray, pink, and orange colors, respectively (Figure S2). After performing 10 ps AIMD simulations at 298 K, the Ag₁₅ framework further increased its deformation, but it could still maintain the overall octahedral configuration. Meanwhile, 4 out of the 12 alkynyl ligands spontaneously broke one Ag–C bond and transformed from μ_3 coordination into the μ_2 configuration. Thus, when the Ag₁₅ NC is exposed to an alkaline electrolyte environment, the architecture of its metal core can remain stable, whereas the local coordination modes of some surface ligands may fluctuate due to the interfacial traction exerted by the solvation effect. Of note, the Ag₁₅ cluster also exhibited similar structural flexibility in a pure water environment (Figure S3). Some silver atoms in the metal core underwent slight displacements, and some of the surface M–C bonds broke, resulting in a decrease in the overall symmetry of the cluster. These results indicate the dynamic structural changes of the cluster in the aqueous environment.

Beyond the solvation effect, the electrical potential plays a more critical role in electrochemical kinetics. However, assessing the system potential is challenging because the zero-dimensional clusters inherently lack a theoretically ideal flat electrode. The experimental protocols typically involve mixing such cluster catalysts with carbon powder to form an ink, which is subsequently loaded onto a glassy carbon electrode. Therefore, to ensure that the simulation strategy mimics the experiment, constant-potential explicit-solvation molecular dynamics simulations were performed using a solid-electrolyte-Ne double electrode model. The explicit solvent is used to simulate the dynamic interactions between solvent molecules and the cluster, and the constant potential is employed to mimic the solid–liquid interfacial microenvironment, enabling the investigation of the electrochemical reactions. As shown in Figure S4, an Ag₁₅ NC molecule was placed within a cubic periodic cell (25 Å × 25 Å × 45 Å). A monolayer of graphene with fixed C atoms was then constructed ~5 Å below the cluster, where only noncovalent interactions (Figure S5) exist between the two to collectively represent the simulated electrode. The space above the electrode surface was filled with 250 water molecules at a density of 1 g cm⁻³. The alkali metal Na⁺ cation was initially positioned ~5 Å away from the catalyst surface, while the anion F⁻ was placed far away on the other side of the solvent to form an ionization pair with the cation, in order to keep the applied potential close to the CO₂RR potential. An additional Ne atomic layer of fixed Ne atoms and a 12 Å vacuum layer were added over the interface model, serving as a counter electrode to prevent penetration of the water layer below the electrode during simulation and to monitor the electrochemical potential of the entire system, as proposed by Surendralal et al.^{40,41} A dipole correction was applied along the direction perpendicular to the interface within the vacuum layer. The applied potential (U vs SHE) can be calculated

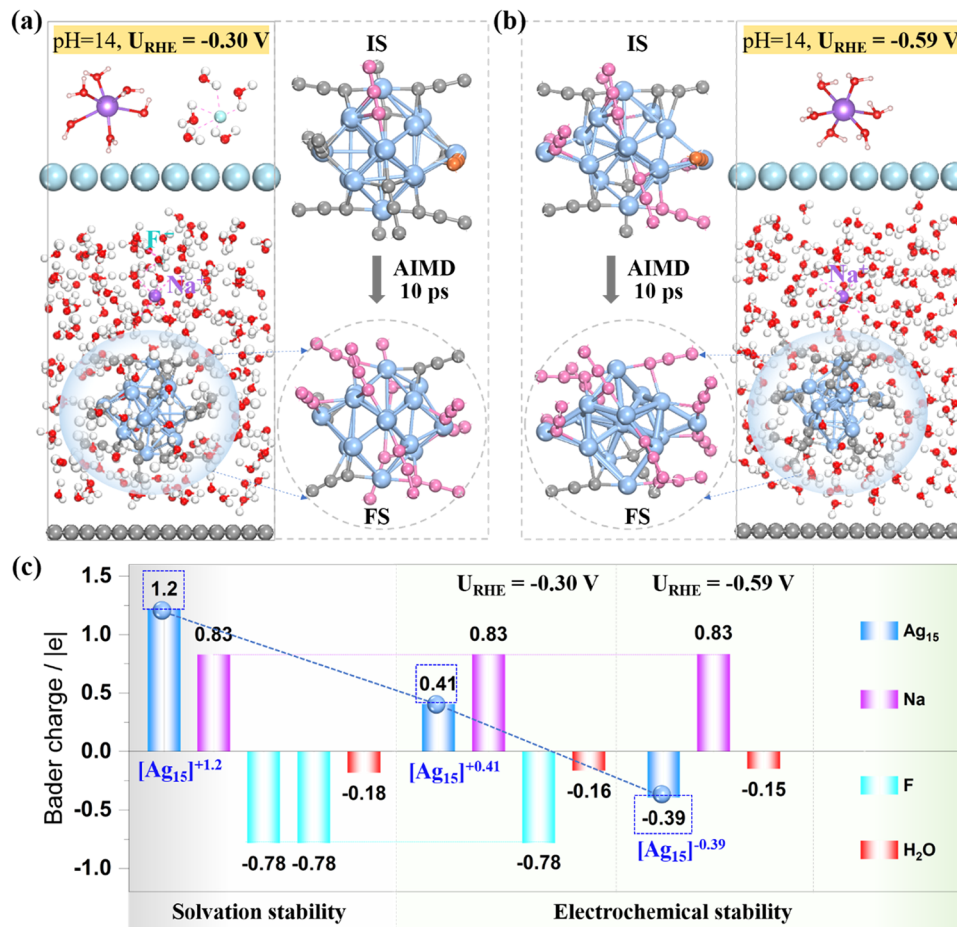


Figure 1. AIMD snapshots of the Ag_{15} NC at electrode potential of (a) $\text{U}_{\text{RHE}} = -0.30 \text{ V}$ and (b) $\text{U}_{\text{RHE}} = -0.59 \text{ V}$ in an alkaline system. (c) Bader charge results of key components (Na^+ , F^- , and the Ag_{15} cluster). Color code: Ag, blue; Na, purple; F, cyan; C, gray/pink/orange; Ne, light blue; O, red; and H, white.

based on the formula $U = \Phi_{\text{Interface}} - 4.44 \text{ V}$, where $\Phi_{\text{Interface}} = \Phi_{\text{Graphene}} + 4\pi\mu k/A$. Here, Φ denotes the work function of the interface or the graphene side, μ is the system's dipole moment, A is the surface area, and k is the Coulomb constant. As shown in Figure 1a,1b, we carried out unrestricted AIMD simulations at 298 K under two constant potentials (-0.30 V and -0.59 V). Clearly, as the potential becomes more negative, the deformation of the metal core becomes greater, and nearly 10 of the surface alkynyl ligands have partial Ag–C bonds breaking and transforming into the stable μ_2 coordination forms (highlighted by the pink C atoms). Hence, the electrical potential will further exacerbate the distortion of the metal core and modulate the Ag–C interface microenvironment. It is worth noting that in the aqueous solution, both Na^+ and F^- ions form stable solvation shells, which are coordinated with six water molecules. The Bader charge analysis reveals that each Na and F ion carries approximately 0.8 positive or negative charges, indicating the effective solvation (Figure 1c). Moreover, considering the solvation stability, the Ag_{15} NC surface carries approximately +1.2 lel in the alkaline solution, consistent with the experimentally determined +1 oxidation state. However, under the electrochemical reduction conditions, the Ag_{15} NC surface gradually acquires a partial negative charge as the applied potential becomes increasingly negative (from +0.41 lel at -0.30 V to -0.39 lel at -0.59 V , Figure 1c). These results imply that the dynamic restructuring

of the Ag_{15} catalyst, such as the gradually exposed Ag metal core due to the partial Ag–C bond cleavage and the accumulated negative electrons on the surface, favors the catalytic process of CO_2RR , although the cluster stability becomes a concern.

Recent experimental studies have successfully synthesized Ag_{15} doped NCs, such as metal-doped $[\text{Ag}_8\text{Au}_7(\text{C}\equiv\text{C}-\text{t-Bu})_{12}]^+$ (Ag_8Au_7) and $[\text{Ag}_9\text{Cu}_6(\text{C}\equiv\text{C}-\text{t-Bu})_{12}]^+$ (Ag_9Cu_6), and the nonmetal-doped $[\text{Ag}_{14}\text{Cl}(\text{C}\equiv\text{C}-\text{t-Bu})_{12}]^+$ (Ag_{14}Cl).^{9,12} The single-crystal X-ray diffractometer analyses revealed that the synthesized Ag_9Cu_6 NC adopted a core–shell–shell configuration of $\text{Ag}_1@\text{Ag}_8@\text{Cu}_6$ similar to that of Ag_8Au_7 NC, as both of them can be classified as body-centered cubic based M_{15}^+ series with an M_1 kernel@ Ag_8 cube@ M_6 octahedron architecture. The Ag_{14}Cl NC was composed of a central Cl atom surrounded by an Ag_8 cube and an Ag_6 octahedral cage (Figure S6). The frameworks of these four clusters were all protected with 12 alkynyl ligands, forming six $\text{t-BuC}\equiv\text{C}-\text{M}-\text{C}\equiv\text{C}-\text{t-Bu}$ motifs. Despite their structural similarity, these doped clusters exhibit differing catalytic activity for the CO_2RR . This naturally raises a critical question: does such intrinsic doping effectively enhance the structural stability of the clusters under electrochemical operating conditions or further modulate their reactivity compared to the pristine Ag_{15} NC? To clarify this, we further investigated the influence of Au, Cu, and Cl atom doping on the dynamic electrochemical

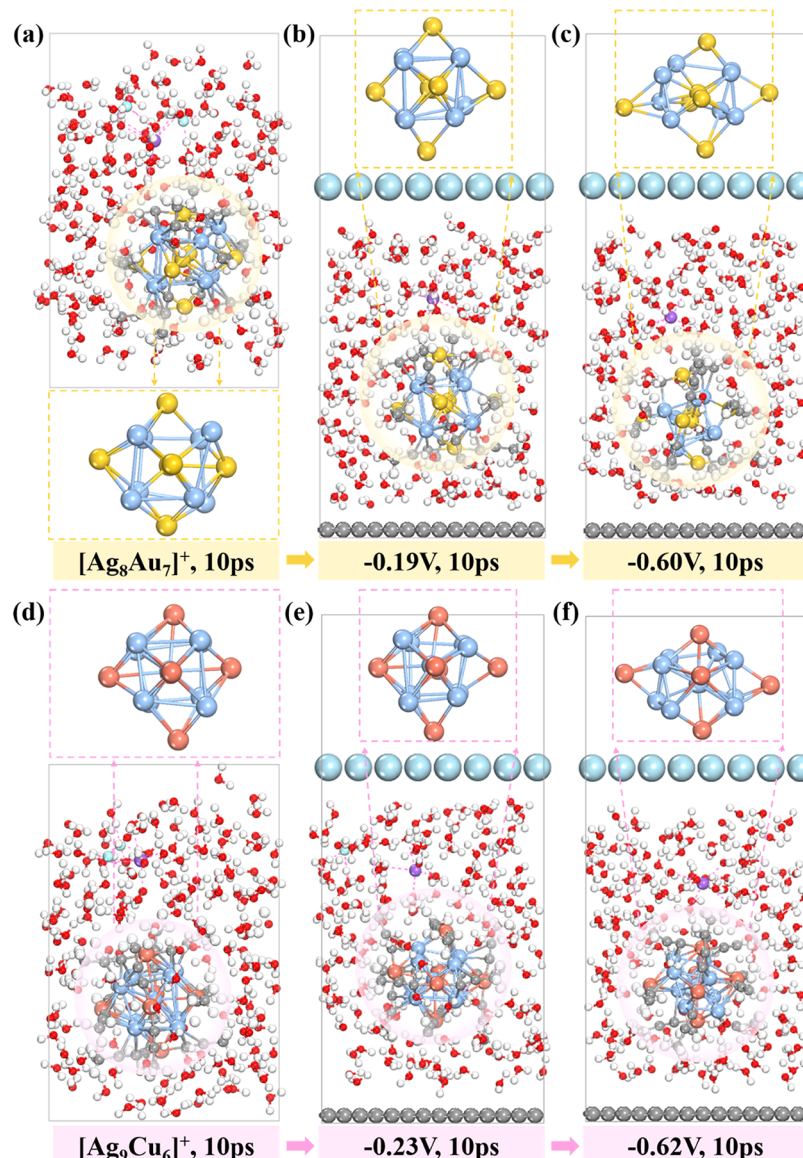


Figure 2. AIMD snapshots of the (a–c) Ag_8Au_7 NC and (d–f) Ag_9Cu_6 NC at 298 K in an alkaline system without applied potential and under two different negative potentials. Color code: Ag, blue; Au, gold; Cu, orange; Na, purple; F, cyan; C, gray; Ne, light blue; O, red; and H, white.

stability of the Ag_{15} NC. Gold and copper were selected as representative metal dopants to evaluate the electronic effects and geometric perturbations. Chlorine, a typical nonmetal dopant, is expected to induce significant charge redistribution due to its strong electronegativity. By comparing these three representative doped systems, we aim to elucidate the distinct contributions of the dopant character to the structural integrity and dynamic stability of the Ag_{15} NC during electrochemical cycling, thereby providing a theoretical basis for understanding the structure–stability relationships governing the doping effects. After 10 ps AIMD simulations, we found that the core structures of these doped clusters exhibit significant distortion (Figures 2 and 3). Notably, as the applied potential shifts negatively, the distortion of the initially regular octahedral structure intensifies (Figure S7 vs Figures 2 and 3), accompanied by significantly increased Ag–C bond dissociation in the surface-coordinated alkynyl ligands. These ligands progressively transform into μ_2 (highlighted by pink) or μ_1 (highlighted by orange) coordination modes (Figure S7). Among these studied clusters, the $Ag_{14}Cl$ core exhibits the

most pronounced deformation, suggesting the lowest dynamic structural stability under simulated electrochemical conditions (Figure 3a,3b). Similarly, Bader charge analysis further confirms the effective solvation of Na^+ cations and F^- anions within the solvent environment (Figure 3c). In the absence of an applied potential, the cluster system maintains an average charge state of approximately +1 lel. As the potential shifts negatively, the negative charge progressively accumulates on the cluster surface. This potential-dependent charge evolution clearly demonstrates the efficacy of the employed double electrode explicit solvation model in modulating the electrochemical potential of the cluster system.

Constrained AIMD Simulations. The above unconstrained AIMD simulations reveal significant core distortion and partial Ag–C bond cleavage in surface alkynyl ligands across all four cluster systems. However, complete ligand desorption was not observed within the short simulation time frame. Lee and their co-workers have experimentally confirmed that alkynyl ligands can fully dissociate on relevant electrochemical time scales.^{9,42} To probe the possibility of complete

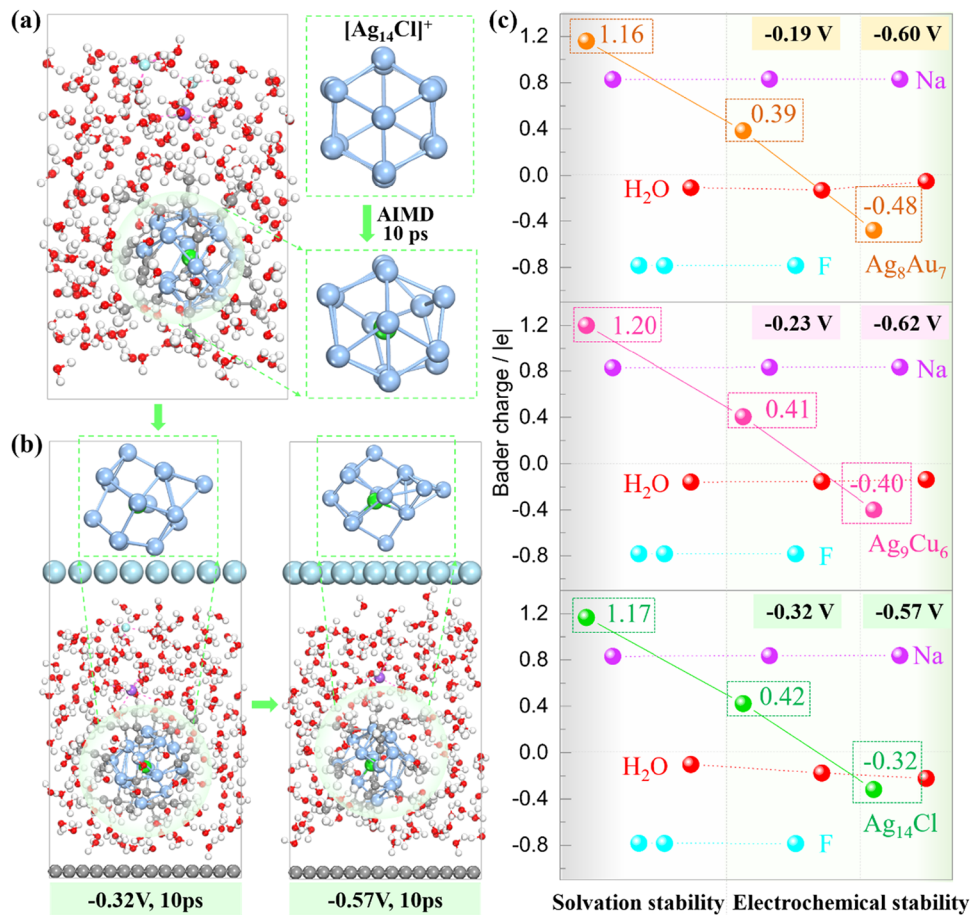


Figure 3. AIMD snapshots of the $Ag_{14}Cl$ NC at 298 K in an alkaline system without an applied potential (a) and under two different negative potentials (b). (c) Bader charge analyses of the key components for Ag_8Au_7 , Ag_9Cu_6 , and $Ag_{14}Cl$. Color code: Ag, blue; Cl, green; Na, purple; F, cyan; C, gray; Ne, light-blue; O, red; and H, white.

alkynyl desorption and quantify its kinetic barrier, we then performed constrained *ab initio* molecular dynamics (cAIMD) simulations at a potential of approximately -0.6 V based on the equilibrium configuration obtained from the aforementioned AIMD simulations. The ligand desorption would proceed via three primary protonation-mediated pathways, as illustrated in Figure 4a. For case 1, the H from a solvent water molecule directly attacks the terminal carbon atom of the alkynyl ligand, ultimately forming propyne ($HC\equiv CCH_3$) and enabling its complete desorption from the metal surface. The collective variable (CV) is defined by $CV = d_1 - d_2 = lr_O - r_H - lr_H - r_C$, where r_C refers to the coordinate of the terminal carbon atom, r_O refers to the coordinate of the O atom on H_2O , and r_H refers to the coordinate of the H atom on H_2O . For case 2, a proton from a neighboring water molecule initially attacks a metal atom, which subsequently transfers to the terminal carbon atom of the alkynyl ligand, leading to the $HC\equiv CCH_3$ formation and its complete desorption. The CV is defined by $CV = d_1 - d_2 = lr_O - r_H - lr_H - r_M$, where r_M refers to the coordinate of the metal atom, while r_H and r_O , respectively, represent the coordinates of the H and O atoms in the adjacent water molecule. For case 3, initially, one M–C bond is constrained to cleave ($CV = d_1$). Should incomplete ligand detachment occur, an additional M–C bond is then restricted to rupture ($CV = d_2$). The resulting detached alkynyl fragment subsequently abstracts a H from a solvent

H_2O to form $HC\equiv CCH_3$, ultimately achieving its detachment from the metal surface.

The dynamic sampling results of the four clusters for case 1 (Figure 4b–e) revealed that the H in H_2O gradually separates with the elongation of the H–O bond and is eventually migrated to the terminal alkyne C atom. However, the limited 4 ps simulation time at 298 K proved insufficient to induce complete ligand desorption. Consequently, we further quantified the dissociation energy of the M–C coordination bonds. The final free-energy profiles reveal that the alkynyl ligands on the Ag_{15} , Ag_7Au_8 , and $Ag_{14}Cl$ surfaces undergo highly facile desorption at low energy barriers (≤ 0.6 eV, see the summary of case 1 in Table 1). In contrast, the desorption process is significantly suppressed on the Ag_9Cu_6 surface due to its strong Cu–C bonding strength, exhibiting a substantially higher ligand desorption barrier of 1.4 eV. Moreover, the kinetic sampling results for case 2 (Figures S8a,c and S9a,c) reveal that the H dissociated from water molecules spontaneously migrates to the terminal carbon atom of a neighboring alkynyl ligand after adsorbing onto a metal site. Dynamic free-energy analysis further demonstrates that only alkynyl ligands on the Ag_{15} and Ag_8Au_7 surfaces achieve low-barrier desorption (< 0.2 eV, see the summary of case 2 in Table 1). Nevertheless, the desorption barriers for ligands in the other two cluster systems significantly increase (≥ 1.7 eV), likely originating from the doping-induced local reinforcement effects: (1) the dynamically enhanced M–C (M = Cu/Ag)

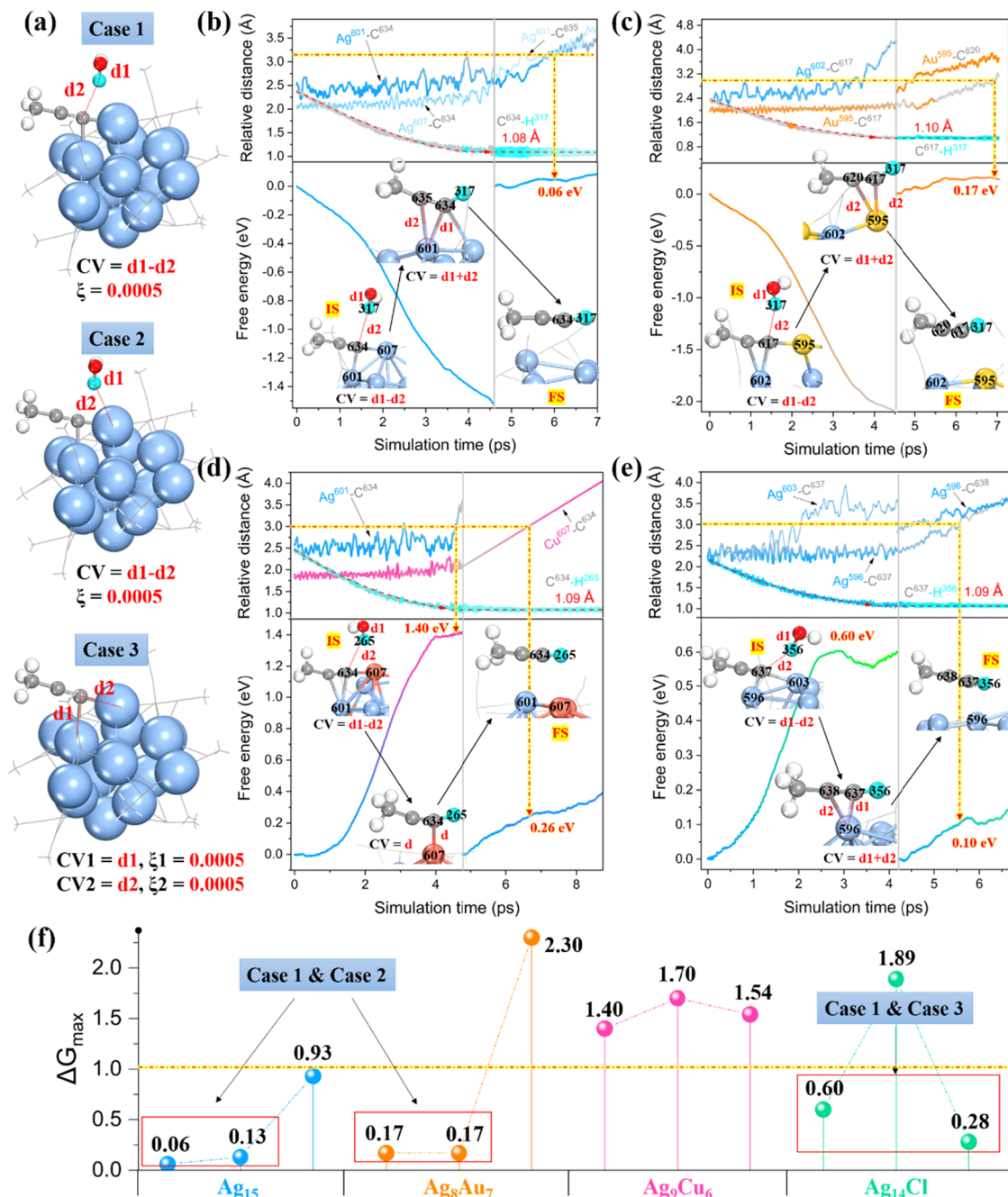


Figure 4. (a) Schematic of three possible kinetic reaction pathways for alkynyl ligand desorption. Free-energy profiles for ligand desorption via case 1 on (b) Ag_{15} , (c) Ag_8Au_7 , (d) Ag_9Cu_6 , and (e) Ag_{14}Cl during the cAIMD simulation at $U_{\text{RHE}} \approx -0.6$ V. The local structural details concerning the initial and final states are denoted as IS and FS, respectively. (f) Comparative summary of all kinetic energy barriers in different nanocluster systems. Color code: Ag, blue; Au, gold; Cu, orange; Cl, green; C, gray; O, red; and H, white.

Table 1. Summary of the Kinetic Energy Barriers (eV) of Alkynyl Desorption for Four Types of NCs in Three Different Cases

NC	case 1	case 2	case 3
Ag_{15}	0.06 (<0.6)	0.13 (<0.2)	0.93 (>0.90)
Ag_8Au_7	0.17 (<0.6)	0.17 (<0.2)	2.30 (>0.90)
Ag_9Cu_6	1.40	1.70 (≥ 1.70)	1.54 (>0.90)
Ag_{14}Cl	0.60 (≤ 0.6)	1.89 (> 1.70)	0.28

bonding suppresses H transfer to the metal and (2) the restructured hydrogen-bonding networks impede dissociation

of the reactive H_2O molecule. Evidently, ligands on these two NC surfaces cannot undergo dynamic desorption via the designated metal-mediated hydrogen transfer pathway. Assuming the preferential cleavage of the M–C bonds over H transfer from water to the terminal alkyne carbon (pathway for case 3), the dynamic free-energy profiles in Figures S8b,d and S9b,d demonstrate effective desorption solely for alkynyl ligands on the Ag_{14}Cl surface with a small barrier of 0.28 eV, whereas the other three systems exhibit substantially higher energy barriers (>0.9 eV, see the summary of case 3 in Table 1). For comparison, the energy barriers obtained from all of the integrated cAIMD simulations (Figure 4f) reveal distinct

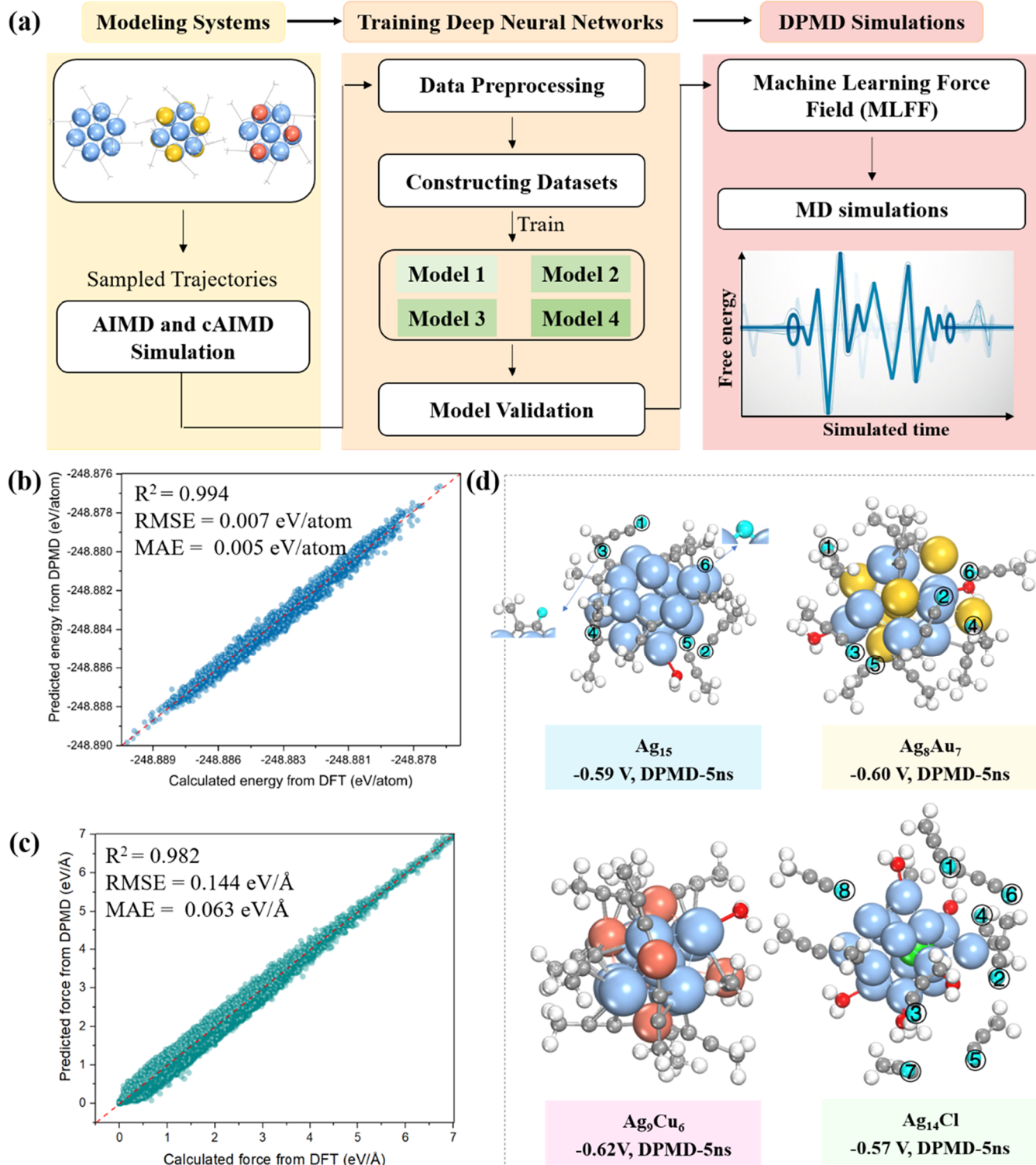


Figure 5. (a) Schematic illustration of the workflow of DPMD simulations. The comparison between the atomic energies (b) and forces (c) of Ag_{15} NC predicted by the generated MLFF model and calculated from DFT. The insets represent the errors toward atomic energies (unit: eV) and forces (unit: $\text{eV} \text{\AA}^{-1}$) for validation data. (d) The balanced DPMD snapshots at 5000 ps of the Ag_{15} , Ag_8Au_7 , Ag_9Cu_6 , and Ag_{14}Cl NCs at $U_{\text{RHE}} \approx -0.6$ V. Color code: Ag, blue; Au, gold; Cu, orange; Cl, green; C, gray; O, red; and H, white.

preferences for ligand desorption: the alkynyl ligands on Ag_{15} and Ag_8Au_7 surfaces preferentially undergo desorption via case 1 and 2 pathways; those on Ag_{14}Cl NC favor case 1 and 3 pathways; while the Ag_9Cu_6 NC exhibits no significant ligand desorption. These findings collectively demonstrate that dopants can effectively modulate the structural dynamics

behavior of silver-based clusters under electrochemical conditions.

DPMD Simulations. So far, our computational modeling of the dynamic behavior for the four silver-based NCs has revealed a consistent transition from the initial octahedral configuration toward disordered frameworks under electro-

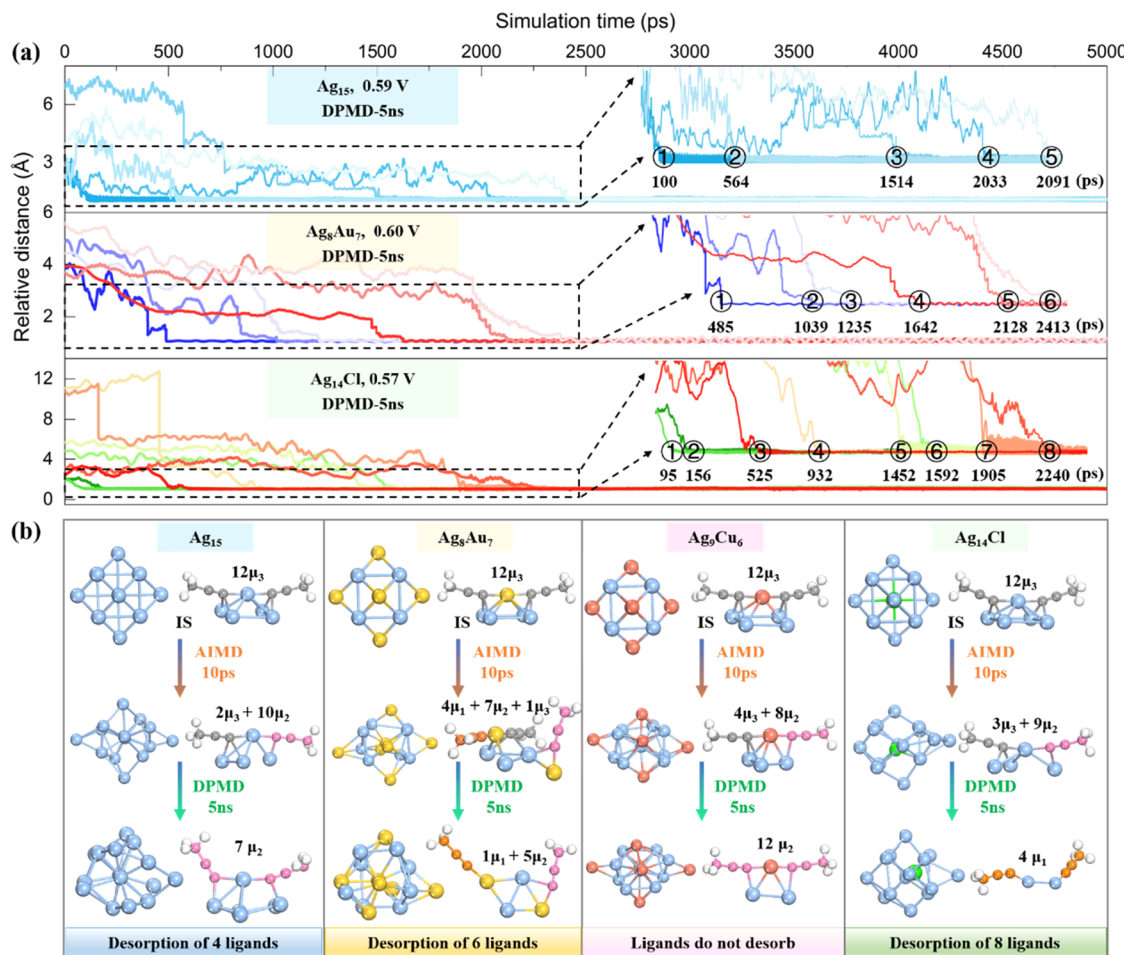


Figure 6. (a) Dynamic changes of H moving from the water layer to the terminal C atom over time during the DPMD simulation, along with the detailed enlargement of local structures. (b) Comparison of local atomic details between the initial configuration and the dynamic equilibrium structure. Color code: Ag, blue; Au, gold; Cu, orange; Cl, green; C, gray/pink/orange; and H, white.

chemical reduction conditions. However, due to the computationally prohibitive cost of high-precision AIMD simulations, the collective stripping of alkynyl ligands at the metal–ligand interface was not observed within the limited simulation time frame. Even with enhanced local reaction sampling via cAIMD methods, only single-ligand desorption events can be captured. To overcome the short time-scale bottleneck and achieve long-range structure evolution in a realistic electrochemical environment, we developed a machine learning force field (MLFF) based on the deep neural network frameworks. This approach maintains near-DFT accuracy while extending simulations to the nanosecond regime, permitting systematic investigation of the cluster structural evolution in critical dynamic processes.

Figure 5a illustrates the workflow for conducting deep potential molecular dynamics (DPMD) simulations. Our workflow consists of three main steps: initialization, training, and MD simulation. Creating an accurate MLFF requires collecting data from DFT calculations to cover as many configurations in the phase space as possible. The initial data are based on the approximately 30,000 AIMD configurations that already exist for each cluster system, along with their energies and forces as labels. For structures where MLFF predictions were not accurate enough, we relabeled these structures using self-consistent DFT calculations and reintegrated them into the data set. In the training step, for each

investigated system, four distinct MLFF models were independently trained. Rigorous convergence verification and error analysis systematically validated the reliability of each model. The root-mean-squared-error (RMSE) and mean-absolute-error (MAE) of predicted energies by MLFF are <0.01 eV per atom, and the RMSE and MAE of predicted atomic forces are about <0.15 eV Å⁻¹ for all systems (Figures 5b,c and S10). These results indicate that the constructed MLFF achieves *ab initio*-level accuracy in fitting both forces and energies, enabling direct simulation of dynamic behavior. Furthermore, to specifically evaluate its reliability in the crucial catalytic region, we separately calculated the force errors for the nanocluster and water atoms. As shown in Figure S11, the MLFF demonstrates exceptional accuracy for both the nanocluster and the water solvent, confirming its reliability in the AIMD simulations of the cluster–solvent interface. Moreover, to evaluate the generalization capability of the MLFF in long-time scale simulations, we performed a post-hoc validation analysis. Two independent data sets were extracted from the 5 ns DPMD trajectory of the Ag_{15} system: (i) Data set A (Global Sampling), comprising 500 frames randomly selected from the equilibrated trajectory; and (ii) Data set B (Critical Sampling), containing 300 transient frames involving the breaking/forming of Metal–CCCH₃ or HO–H bonds. As shown in Figure S12, our MLFF maintained high predictive accuracy with only a slight increase in the RMSE and MAE

forces, well below the commonly accepted threshold for reliable qualitative AIMD conclusions (~ 0.3 eV/ \AA). This indicates that the model has successfully captured the fundamental physics of bond reactions and retains excellent extrapolation capability.

Leveraging this high-accuracy MLFF, we then extended the dynamic evolution of the four silver-based NCs to the nanosecond regime, revealing for the first time their long-time scale structural reorganization and ligand dissociation kinetics. At an applied potential of approximately -0.6 V, we sampled approximately 5 million configurations from the DPMD trajectories for each system, equivalent to 5000 ps of simulation time. In the DPMD simulations, we observed that all of the cluster systems undergo a disordered structural evolution of the metal core. Particularly, multiple ligand desorption occurred on the surface of all NCs except for Ag_9Cu_6 (Figure Sd). Specifically, six H atoms are found to migrate from the aqueous layer to the surface of the Ag_{15} system. Among them, four H atoms are stably bonded to the terminal C atom of the alkyne groups, driving complete dissociation of the corresponding ligands. One H (labeled as No. 3) bonds to a terminal C atom but remains anchored to the Ag surface in a nonlinear configuration due to the enhanced ligand restraint from the exposed metal sites. Another H atom (labeled as No. 6) adsorbs in a bridging position between two Ag atoms, which is a plausible consequence of the increased reactive space following ligand removal. In the Ag_8Au_7 system, all of the six migratory H atoms are stably bonded to the terminal carbon of the alkynyl groups, driving the complete desorption of six alkynyl ligands. Moreover, in the Ag_{14}Cl system, up to 8 alkynyl ligands are completely desorbed at the metal–ligand interface. However, no ligand desorption was observed in the Ag_9Cu_6 system, which is consistent with the prior kinetic barrier predictions. Interestingly, these clusters share a common feature: all systems exhibit the exposure of metal sites due to ligand dissociation/bond breaking, which in turn triggers the adsorption of water molecules that might imply the risk of surface oxidation for the NCs. Among the four investigated NCs, the Ag_{14}Cl system shows the highest water adsorption on its surface (correlating with its maximal ligand desorption), suggesting its weakest structural stability. Furthermore, we systematically analyzed the fate of the OH species following all water dissociation events. As shown in Figure S13, three primary states were observed: (1) existence as a solvated hydroxide ion (OH^-) within the aqueous layer; (2) formation of a transient proton-shared dimer ($\text{H}_2\text{O}\cdot\text{OH}^-$) with a water molecule; and (3) stable presence as an adsorption species ($^*\text{OH}$) on the surface of the Ag_{14}Cl NC. It is noteworthy that the adsorbed $^*\text{OH}$ species may cause local oxidation of the cluster surface. These results strongly demonstrate that the OH species generated from water dissociation follow diverse reaction pathways. Their final state is highly dependent on the local atomic environment and the electrochemical potential, indicating the complex kinetic behavior of the water dissociation process at the interface.

To facilitate the tracking of the dissociation kinetics, we further analyzed in detail the dynamics of H moving from the water layer to the terminal C atom during the simulation. Figure 6a indicates that Ag_{14}Cl NC achieves fast proton bonding at the earliest time (95 ps), followed by Ag_{15} (100 ps) and Ag_8Au_7 (485 ps). And only after a DPMD simulation duration of at least 2000 ps can the maximum number of

surface ligands be removed. After that, no further ligand desorption can be monitored within the extended 5000 ps DPMD simulations, confirming the maximum loss of 4, 6, and 8 ligands for Ag_{15} , Ag_8Au_7 , and Ag_{14}Cl NCs, respectively, at this potential. By comparing all of the kinetic results (Figure 6b), we observe that during the simulation process, the core of the NCs will definitely evolve toward amorphization, with atomic disordering intensifying over time; while at the interface, the partial/full Ag–C bond cleavage in surface ligands is inevitable. Particularly, the residual ligands adopt bidentate coordination on Ag_{15} and Ag_9Cu_6 NCs versus monodentate coordination on Ag_{14}Cl NC. The above analysis quantitatively elucidates the long-time scale structure evolution mechanisms of Ag NCs in the electrochemical environments: (1) the core disordering and ligand desorption are ubiquitous; (2) the ligand dissociation kinetics are dopant-regulated, with the desorption capacity and the saturation time being cluster-specific; and (iii) ≥ 2000 ps simulations are necessary to capture the realistic electrochemical dynamic stability.

To clarify the physical origin of the influence of doping on ligand dissociation, we conducted a systematic electronic structure analysis. As shown in Table S1, as the ligands gradually break, the Bader charge of the metal cluster becomes more negative, and the d-band center systematically shifts upward. These trends are particularly significant in clusters with more ligand desorption. This phenomenon indicates that ligand dissociation induces the reflow of electrons from the ligands to the metal framework, and the upward shift of the d-band center indicates an enhancement of the interaction between the metal and the adsorbate, rendering the cluster surface with higher reactivity. These electronic structure changes have a crucial effect on the catalytic behavior of CO_2 reduction. The ligand dissociation directly exposes the metal sites, providing a necessary site for the CO_2 adsorption. More importantly, the upward shift of the d-band center and the surface charge enrichment can jointly enhance the CO_2 activation. The upward shift of the d-band center strengthens the coupling between metal d orbitals and the π^* antibonding orbital (LUMO) of CO_2 , thereby weakening the $\text{C}=\text{O}$ bond. At the same time, the electron-rich surface is more likely to inject an electron into the LUMO orbital of CO_2 , stabilizing the adsorbed state and reducing the reaction barrier. Based on this, we speculate that the CO_2 reduction activity follows the order $\text{Ag}_{14}\text{Cl} > \text{Ag}_8\text{Au}_7 > \text{Ag}_{15} > \text{Ag}_9\text{Cu}_6$. Among them, the Ag_{14}Cl cluster with higher ligand dissociation not only has more exposed active sites but also has higher intrinsic site activity. However, a higher reactivity could be accompanied by a decrease in electrochemical stability, which is particularly significant in the Ag_{14}Cl system.

CONCLUSIONS

This study elucidates the dynamic structural evolution mechanisms of alkynyl-protected atomically precise Ag NCs under electrochemical reduction conditions through multiscale molecular simulations. We revealed that all NCs would undergo metal–core distortion and surface ligand reorganization, with the applied potential driving the transition of partial alkynyl ligands from μ_3 to μ_2/μ_1 coordination modes, accompanied by the solvation-induced charge redistribution. The dopants significantly modulate the kinetics by regulating the metal–ligand bond strength: the metal Cu doping enhances the Ag_9Cu_6 cluster stability, while the nonmetallic Cl doping can induce accelerated degradation in Ag_{14}Cl ; the

Au doping facilitates facile and moderate ligand desorption. Crucially, the 5000 ps DPMD simulations finally revealed that the partial or complete dissociation of Ag–C bonds in alkynyl ligands for subsequent detachment is an inevitable outcome of the long-term structure evolution. There is a saturation threshold for ligand desorption, requiring at least 2000 ps to approach the steady state. The metal sites exposed during this dynamic process, although beneficial for the electrocatalytic activity, may simultaneously trigger water adsorption and pose surface oxidation risks, which is particularly pronounced in the Ag_{14}Cl NC with the possibility of maximal ligand desorption. Overall, by overcoming the AIMD time scale limitations, this work achieves nanosecond-scale dynamic resolution with near-DFT accuracy, providing atomic-level mechanisms for rationally designing high-stability silver-based NC catalysts.

■ EXPERIMENTAL SECTION

AIMD Simulations. All *ab initio* molecular dynamics simulations based on first-principles theory were performed by employing the QUICKSTEP program of the CP2K package.⁴³ The spin-polarized electronic structure calculations are described by Perdew–Burke–Ernzerhof (PBE) functional and mixed double- ζ Gaussian and plane-wave (GPW) basis sets with a plane-wave basis set and an energy cutoff of 350 Ry.⁴⁴ The core electrons of Ag, Au, Cu, Ne, C, Na, Cl, F, O, and H atoms are modeled by Goedecker–Teter–Hutter (GTH)-type pseudopotentials.⁴⁵ Long-range van der Waals interactions are treated using the DFT-D3 dispersion correction.⁴⁶ Simulations were carried out within the NVT canonical ensemble using a Nosé–Hoover thermostat (298 K) and a 1 fs integration step.^{47,48} Only the γ -centered k-mesh was adopted in the AIMD simulations. Considering the fluctuation of the work function, at least one snapshot was extracted from the AIMD trajectory every 500 frames to finally determine the corresponding average potential. The detailed calculation of electrode potential in the unconstrained AIMD method has been documented in the [Results and Discussion](#) section.

To calculate the kinetic barriers of alkynyl ligand desorption, the constrained AIMD simulations with a thermodynamic integration (TI) approach^{49,50} were applied as implemented in CP2K to obtain the free-energy profile. These values were derived by constraining the reaction coordinate variable (CV, ζ ; defined in [Figure 4a](#)) during cAIMD runs, employing a CV displacement rate ($d\zeta$) of 0.0005 Å for each constrained AIMD step. Moreover, we employ the average value of the potentials at the initial state (U_{IS}) and final state (U_{FS}) as the potential (U_r) of the cAIMD protocol with enhanced sampling (i.e., $U_r = (U_{\text{IS}} + U_{\text{FS}})/2$).^{51,52} Then, the free energy for constant potential was corrected according to the method proposed by Nørskov et al. ($(\Delta E + \Delta q^* \Delta U)/2$; $\Delta U = U_{\text{IS}} - U_{\text{FS}}$; Δq is the variation of surface charge during reaction).^{53,54}

Model Training and DPMD Simulations. DeePMD-kit software⁵⁵ was used to fit the neural network for atomic interactions within a deep-learning framework. The embedding network featured three hidden layers (25, 50, and 100 nodes), while the fitting network employed three 240-node layers. A 6.0 Å cutoff radius was implemented. The learning rate was initialized at 0.001 and decayed exponentially every 5000 steps, reaching 3.51×10^{-8} after 4,000,000 training cycles, with start and limit scaling factors of energy and force set at 0.02, 1, 1000, and 1, respectively. Four MLFF models are trained here with the same network architecture but a different random initial seed. All DPMD simulations based on MLFF were performed utilizing the LAMMPS code within the NVT ensemble, without any fixed atoms.⁵⁶ A 1 fs time step was employed for all runs. Comprehensive computational model details are available in the [Supporting Information](#).

■ ASSOCIATED CONTENT

SI Supporting Information

The Supporting Information is available free of charge at <https://pubs.acs.org/doi/10.1021/jacs.Sc15207>.

Theoretical model; evolution of the coordination modes; free-energy profiles for ligand desorption pathways; and comparison between MLFF model and DFT ([PDF](#))

■ AUTHOR INFORMATION

Corresponding Author

Qing Tang – School of Chemistry and Chemical Engineering, Chongqing Key Laboratory of Chemical Theory and Mechanism, Chongqing University, Chongqing 401331, China; orcid.org/0000-0003-0805-7506; Email: qingtang@cqu.edu.cn

Author

Fang Sun – Chongqing Key Laboratory of Green Catalysis Materials and Technology, College of Chemistry, Chongqing Normal University, Chongqing 401331, China

Complete contact information is available at: <https://pubs.acs.org/10.1021/jacs.Sc15207>

Notes

The authors declare no competing financial interest.

■ ACKNOWLEDGMENTS

This work was supported by the National Natural Science Foundation of China (Nos. 22503011 and 22473017) and the Chongqing Science and Technology Commission (CSTB2025NSCQ-GPX0998 and CSTB2024NSCQ-MSX0250).

■ REFERENCES

- Jin, R.; Li, G.; Sharma, S.; Li, Y.; Du, X. Toward Active-Site Tailoring in Heterogeneous Catalysis by Atomically Precise Metal Nanoclusters with Crystallographic Structures. *Chem. Rev.* **2021**, *121*, 567–648.
- Shen, H.; Zhu, Q.; Xu, J.; Ni, K.; Wei, X.; Du, Y.; Gao, S.; Kang, X.; Zhu, M. Stepwise construction of Ag_{29} nanocluster-based hydrogen evolution electrocatalysts. *Nanoscale* **2023**, *15*, 14941–14948.
- Tang, Y.; Sun, F.; Ma, X.; Qin, L.; Ma, G.; Tang, Q.; Tang, Z. Alkynyl and halogen co-protected $(\text{AuAg})_{44}$ nanoclusters: a comparative study on their optical absorbance, structure, and hydrogen evolution performance. *Dalton Trans.* **2022**, *51*, 7845–7850.
- Jo, Y.; Choi, M.; Kim, M.; Yoo, J. S.; Choi, W.; Lee, D. Promotion of alkaline hydrogen production via Ni-doping of atomically precise Ag nanoclusters. *Bull. Korean Chem. Soc.* **2021**, *42*, 1672–1677.
- Mu, C.; Wang, B.; Yao, Q.; He, Q.; Xie, J. Composition-dependent catalytic performance of $\text{Au}_x\text{Ag}_{25-x}$ alloy nanoclusters for oxygen reduction reaction. *Nano Res.* **2024**, *17*, 9490–9497.
- Shi, C.-G.; Jia, J.-H.; Jia, Y.; Li, G.; Tong, M.-L. Bulky Thiolate-Protected Silver Nanocluster $\text{Ag}_{213}(\text{Adm-S})_{44}\text{Cl}_{33}$ with Excellent Electrocatalytic Performance toward Oxygen Reduction. *CCS Chem.* **2023**, *5*, 1154–1162.
- Zou, X. J.; He, S. P.; Kang, X.; Chen, S.; Yu, H. Z.; Jin, S.; Astruc, D.; Zhu, M. Z. New atomically precise M_1Ag_{21} ($\text{M} = \text{Au}/\text{Ag}$) nanoclusters as excellent oxygen reduction reaction catalysts. *Chem. Sci.* **2021**, *12*, 3660–3667.

- (8) Yoo, S.; Yoo, S.; Deng, G.; Sun, F.; Lee, K.; Jang, H.; Lee, C. W.; Liu, X.; Jang, J.; Tang, Q.; Hwang, Y. J.; Hyeon, T.; Bootharaju, M. S. Nanocluster Surface Microenvironment Modulates Electrocatalytic CO₂ Reduction. *Adv. Mater.* **2024**, *36*, No. 2313032.
- (9) Seong, H.; Chang, K.; Sun, F.; Lee, S.; Han, S. M.; Kim, Y.; Choi, C. H.; Tang, Q.; Lee, D. ClAg₁₄(C≡C^tBu)₁₂ Nanoclusters as Efficient and Selective Electrocatalysts Toward Industrially Relevant CO₂ Conversion. *Adv. Sci.* **2024**, *11*, No. 2306089.
- (10) Deng, G.; Kim, J.; Bootharaju, M. S.; Sun, F.; Lee, K.; Tang, Q.; Hwang, Y. J.; Hyeon, T. Body-Centered-Cubic-Kernelled Ag₁₅Cu₆ Nanocluster with Alkynyl Protection: Synthesis, Total Structure, and CO₂ Electroreduction. *J. Am. Chem. Soc.* **2023**, *145*, 3401–3407.
- (11) Li, L.-J.; Luo, Y.-T.; Tian, Y.-Q.; Wang, P.; Yi, X.-Y.; Yan, J.; Pei, Y.; Liu, C. Unveiling the Remarkable Stability and Catalytic Activity of a 6-Electron Superatomic Ag₃₀ Nanocluster for CO₂ Electroreduction. *Inorg. Chem.* **2023**, *62*, 14377–14384.
- (12) Ma, X.; Sun, F.; Qin, L.; Liu, Y.; Kang, X.; Wang, L.; Jiang, D.-e.; Tang, Q.; Tang, Z. Electrochemical CO₂ reduction catalyzed by atomically precise alkynyl-protected Au₇Ag₈, Ag₉Cu₆, and Au₂Ag₈Cu₅ nanoclusters: probing the effect of multi-metal core on selectivity. *Chem. Sci.* **2022**, *13*, 10149–10158.
- (13) Chen, L.; Sun, F.; Shen, Q.; Qin, L.; Liu, Y.; Qiao, L.; Tang, Q.; Wang, L.; Tang, Z. Homoleptic alkynyl-protected Ag₃₂ nanocluster with atomic precision: Probing the ligand effect toward CO₂ electroreduction and 4-nitrophenol reduction. *Nano Res.* **2022**, *15*, 8908–8913.
- (14) Qin, L.; Sun, F.; Ma, X.; Ma, G.; Tang, Y.; Wang, L.; Tang, Q.; Jin, R.; Tang, Z. Homoleptic Alkynyl-Protected Ag₁₅ Nanocluster with Atomic Precision: Structural Analysis and Electrocatalytic Performance toward CO₂ Reduction. *Angew. Chem., Int. Ed.* **2021**, *60*, 26136–26141.
- (15) Liu, L.; Zheng, S.-J.; Chen, H.; Cai, J.; Zang, S.-Q. Tandem Nitrate-to-Ammonia Conversion on Atomically Precise Silver Nanocluster/MXene Electrocatalyst. *Angew. Chem., Int. Ed.* **2024**, *63*, No. e202316910.
- (16) Qin, L.; Sun, F.; Li, M.; Fan, H.; Wang, L.; Tang, Q.; Wang, C.; Tang, Z. Atomically Precise (AgPd)₂₇ Nanoclusters for Nitrate Electroreduction to NH₃: Modulating the Metal Core by a Ligand Induced Strategy. *Acta Phys. -Chim. Sin.* **2025**, *41*, No. 100008.
- (17) Qin, L.; Sun, F.; Gong, Z.; Ma, G.; Chen, Y.; Tang, Q.; Qiao, L.; Wang, R.; Liu, Z.-Q.; Tang, Z. Electrochemical NO₃⁻ Reduction Catalyzed by Atomically Precise Ag₃₀Pd₄ Bimetallic Nanocluster: Synergistic Catalysis or Tandem Catalysis? *ACS Nano* **2023**, *17*, 12747–12758.
- (18) Ma, G.; Sun, F.; Qiao, L.; Shen, Q.; Wang, L.; Tang, Q.; Tang, Z. Atomically Precise Alkynyl-Protected Ag₂₀Cu₁₂ Nanocluster: Structure Analysis and Electrocatalytic Performance toward Nitrate Reduction for NH₃ Synthesis. *Nano Res.* **2023**, *16*, 10867–10872.
- (19) Sun, G.; Sautet, P. Active Site Fluxional Restructuring as a New Paradigm in Triggering Reaction Activity for Nanocluster Catalysis. *Acc. Chem. Res.* **2021**, *54*, 3841–3849.
- (20) Eren, B.; Zherebetsky, D.; Patera, L. L.; Wu, C. H.; Bluhm, H.; Africh, C.; Wang, L.-W.; Somorjai, G. A.; Salmeron, M. Activation of Cu(111) surface by decomposition into nanoclusters driven by CO adsorption. *Science* **2016**, *351*, 475–478.
- (21) Luo, L.; Nian, Y.; Wang, S.; Dong, Z.; He, Y.; Han, Y.; Wang, C. Real-Time Atomic-Scale Visualization of Reversible Copper Surface Activation during the CO Oxidation Reaction. *Angew. Chem., Int. Ed.* **2020**, *59*, 2505–2509.
- (22) Ding, K.; Gulec, A.; Johnson, A. M.; Schweitzer, N. M.; Stucky, G. D.; Marks, L. D.; Stair, P. C. Identification of active sites in CO oxidation and water-gas shift over supported Pt catalysts. *Science* **2015**, *350*, 189–192.
- (23) Herzing, A. A.; Kiely, C. J.; Carley, A. F.; Landon, P.; Hutchings, G. J. Identification of Active Gold Nanoclusters on Iron Oxide Supports for CO Oxidation. *Science* **2008**, *321*, 1331–1335.
- (24) Hu, S.; Li, W.-X. Sabatier principle of metal-support interaction for design of ultrastable metal nanocatalysts. *Science* **2021**, *374*, 1360–1365.
- (25) Wang, Z. W.; Palmer, R. E. Experimental Evidence for Fluctuating, Chiral-Type Au₅₅ Clusters by Direct Atomic Imaging. *Nano Lett.* **2012**, *12*, 5510–5514.
- (26) Zheng, K.; Fung, V.; Yuan, X.; Jiang, D.-E.; Xie, J. Real Time Monitoring of the Dynamic Intralcluster Diffusion of Single Gold Atoms into Silver Nanoclusters. *J. Am. Chem. Soc.* **2019**, *141*, 18977–18983.
- (27) Cox, B. D.; Woodworth, P. H.; Wilkerson, P. D.; Bertino, M. F.; Reiner, J. E. Ligand-Induced Structural Changes of Thiolate-Capped Gold Nanoclusters Observed with Resistive-Pulse Nanopore Sensing. *J. Am. Chem. Soc.* **2019**, *141*, 3792–3796.
- (28) Takahata, R.; Yamazoe, S.; Maehara, Y.; Yamazaki, K.; Takano, S.; Kurashige, W.; Negishi, Y.; Gohara, K.; Tsukuda, T. Electron Microscopic Observation of an Icosahedral Au₁₃ Core in Au₂₅(SePh)₁₈ and Reversible Isomerization between Icosahedral and Face-Centered Cubic Cores in Au₁₄₄(SC₂H₄Ph)₆₀. *J. Phys. Chem. C* **2020**, *124*, 6907–6912.
- (29) Foster, D. M.; Pavloudis, T.; Kioseoglou, J.; Palmer, R. E. Atomic-resolution imaging of surface and core melting in individual size-selected Au nanoclusters on carbon. *Nat. Commun.* **2019**, *10*, No. 2583.
- (30) Nieto-Ortega, B.; Bürgi, T. Vibrational Properties of Thiolate-Protected Gold Nanoclusters. *Acc. Chem. Res.* **2018**, *51*, 2811–2819.
- (31) Zhang, Z.; Walsh, A. G.; Zhang, P. Dynamic Structure of Metal Nanoclusters from Synchrotron X-ray Spectroscopy. *J. Phys. Chem. C* **2021**, *125*, 5982–5994.
- (32) Sun, Z.; Wang, J.; Su, L.; Gu, Z.; Wu, X.-P.; Chen, W.; Ma, W. Dynamic Evolution and Reversibility of a Single Au₂₅ Nanocluster for the Oxygen Reduction Reaction. *J. Am. Chem. Soc.* **2024**, *146*, 20059–20068.
- (33) Fan, Q.-Y.; Liu, Y.-P.; Zhu, H.-X.; Gong, F.-Q.; Wang, Y.; E, W.; Bao, X.; Tian, Z.-Q.; Cheng, J. Entropy in catalyst dynamics under confinement. *Chem. Sci.* **2024**, *15*, 18303–18309.
- (34) Guo, H.; Sautet, P.; Alexandrova, A. N. Reagent-Triggered Isomerization of Fluxional Cluster Catalyst via Dynamic Coupling. *J. Phys. Chem. Lett.* **2020**, *11*, 3089–3094.
- (35) Kalz, K. F.; Krahnert, R.; Dvoyashkin, M.; Dittmeyer, R.; Gläser, R.; Kreuer, U.; Reuter, K.; Grunwaldt, J. D. Future Challenges in Heterogeneous Catalysis: Understanding Catalysts under Dynamic Reaction Conditions. *ChemCatChem* **2017**, *9*, 17–29.
- (36) Zhou, L.; Fu, X.-P.; Wang, R.; Wang, C.-X.; Luo, F.; Yan, H.; He, Y.; Jia, C.-J.; Li, J.; Liu, J.-C. Dynamic phase transitions dictate the size effect and activity of supported gold catalysts. *Sci. Adv.* **2024**, *10*, No. eadr4145.
- (37) Galib, M.; Limmer, D. T. Reactive uptake of N₂O₅ by atmospheric aerosol is dominated by interfacial processes. *Science* **2021**, *371*, 921–925.
- (38) Shen, Y.; Morozov, S. I.; Luo, K.; An, Q.; Goddard, W. A., III Deciphering the Atomistic Mechanism of Si(111)-7 × 7 Surface Reconstruction Using a Machine-Learning Force Field. *J. Am. Chem. Soc.* **2023**, *145*, 20511–20520.
- (39) Gong, F.-Q.; Liu, Y.-P.; Wang, Y.; E, W.; Tian, Z.-Q.; Cheng, J. Machine Learning Molecular Dynamics Shows Anomalous Entropic Effect on Catalysis through Surface Pre-melting of Nanoclusters. *Angew. Chem., Int. Ed.* **2024**, *63*, No. e202405379.
- (40) Surendralal, S.; Todorova, M.; Neugebauer, J. Impact of Water Coadsorption on the Electrode Potential of H-Pt(111)-Liquid Water Interfaces. *Phys. Rev. Lett.* **2021**, *126* (16), No. 166802.
- (41) Surendralal, S.; Todorova, M.; Finnis, M. W.; Neugebauer, J. First-Principles Approach to Model Electrochemical Reactions: Understanding the Fundamental Mechanisms behind Mg Corrosion. *Phys. Rev. Lett.* **2018**, *120* (24), No. 246801.
- (42) Chen, Y.; Zhou, X.; Liu, X.; Tang, Z.; Wang, L.; Tang, Q. Understanding the Role of Potential and Cation Effect on Electrocatalytic CO₂ Reduction in All-Alkynyl-Protected Ag₁₅ Nanoclusters. *J. Am. Chem. Soc.* **2025**, *147*, 2699–2713.
- (43) VandeVondele, J.; Krack, M.; Mohamed, F.; Parrinello, M.; Chassaing, T.; Hutter, J. Quickstep: Fast and accurate density

- functional calculations using a mixed Gaussian and plane waves approach. *Comput. Phys. Commun.* **2005**, *167*, 103–128.
- (44) Perdew, J. P.; Burke, K.; Ernzerhof, M. Generalized gradient approximation made simple. *Phys. Rev. Lett.* **1996**, *77*, No. 3865.
- (45) Hartwigsen, C.; Goedecker, S.; Hutter, J. Relativistic separable dual-space Gaussian pseudopotentials from H to Rn. *Phys. Rev. B* **1998**, *58*, No. 3641.
- (46) Grimme, S.; Ehrlich, S.; Goerigk, L. Effect of the damping function in dispersion corrected density functional theory. *J. Comput. Chem.* **2011**, *32*, 1456–1465.
- (47) Martyna, G. J.; Klein, M. L.; Tuckerman, M. Nosé–Hoover chains: The canonical ensemble via continuous dynamics. *J. Comput. Chem.* **1992**, *97*, 2635–2643.
- (48) Hoover, W. G. Canonical dynamics: Equilibrium phase-space distributions. *Phys. Rev. A* **1985**, *31*, No. 1695.
- (49) Sprik, M.; Cicotti, G. Free energy from constrained molecular dynamics. *J. Chem. Phys.* **1998**, *109*, 7737–7744.
- (50) Carter, E. A.; Cicotti, G.; Hynes, J. T.; Kapral, R. Constrained reaction coordinate dynamics for the simulation of rare events. *Chem. Phys. Lett.* **1989**, *156*, 472–477.
- (51) Zhao, H.; Cao, H.; Zhang, Z.; Wang, Y.-G. Modeling the Potential-Dependent Kinetics of CO₂ Electroreduction on Single-Nickel Atom Catalysts with Explicit Solvation. *ACS Catal.* **2022**, *12*, 11380–11390.
- (52) Cao, H.; Zhang, Z.; Chen, J.-W.; Wang, Y.-G. Potential-Dependent Free Energy Relationship in Interpreting the Electrochemical Performance of CO₂ Reduction on Single Atom Catalysts. *ACS Catal.* **2022**, *12*, 6606–6617.
- (53) Chan, K.; Nørskov, J. K. Potential Dependence of Electrochemical Barriers from ab Initio Calculations. *J. Phys. Chem. Lett.* **2016**, *7*, 1686–1690.
- (54) Chan, K.; Nørskov, J. K. Electrochemical Barriers Made Simple. *J. Phys. Chem. Lett.* **2015**, *6*, 2663–2668.
- (55) Wang, H.; Zhang, L.; Han, J.; E, W. DeePMD-kit: A deep learning package for many-body potential energy representation and molecular dynamics. *Comput. Phys. Commun.* **2018**, *228*, 178–184.
- (56) Thompson, A. P.; Aktulga, H. M.; Berger, R.; Bolintineanu, D. S.; Brown, W. M.; Crozier, P. S.; in 't Veld, P. J.; Kohlmeyer, A.; Moore, S. G.; Nguyen, T. D.; Shan, R.; Stevens, M. J.; Tranchida, J.; Trott, C.; Plimpton, S. J. LAMMPS - a flexible simulation tool for particle-based materials modeling at the atomic, meso, and continuum scales. *Comput. Phys. Commun.* **2022**, *271*, No. 108171.

CAS BIOFINDER DISCOVERY PLATFORM™

ELIMINATE DATA SILOS. FIND WHAT YOU NEED, WHEN YOU NEED IT.

A single platform for relevant, high-quality biological and toxicology research

Streamline your R&D

CAS 
A division of the
American Chemical Society